Widespread Shocks in the Nucleus of NGC 404 Revealed by Near-infrared Integral Field Spectroscopy

A. Boehle[1,2,6], J. E. Larkin[2], L. Armus[3], and S. A. Wright[4,5]
[1] Institute for Particle Physics and Astrophysics, ETH Zurich, CH-8093 Zurich, Switzerland; boehlea@phys.ethz.ch
[2] Department of Physics & Astronomy, University of California, Los Angeles, CA 90095, USA
[3] IPAC, California Institute of Technology, Pasadena, CA 91125, USA
[4] Department of Physics, University of California, San Diego, CA 92039, USA
[5] Center for Astrophysics and Space Sciences, University of California, San Diego, CA 92039, USA

Abstract

We present high spatial resolution, integral field spectrograph (IFS) observations of the nearby low-ionization nuclear emission-line region (LINER) galaxy NGC 404 at 1.25 μm (J band) and 2.2 μm (K band) near-infrared (NIR) wavelengths. Although NGC 404 is thought to host an intermediate-mass black hole (BH) at its center, it has been unclear whether accretion onto the BH or another mechanism such as shock excitation drives its LINER emission at optical/NIR wavelengths. We use the OSIRIS IFS at Keck Observatory behind laser guide star adaptive optics to map the strength and kinematics of [Fe II], H$_2$, and hydrogen recombination lines at spatial resolutions of 1 pc across the central 30 pc of the galaxy. The H$_2$ gas is in a central rotating disk, and ratios of multiple H$_2$ lines indicate that the molecular gas is thermally excited, with some contribution from UV fluorescence. The [Fe II] emission is more extended and diffuse than the molecular gas and has a different kinematic structure that reaches higher velocities/dispersions. We also map the strength of the CO stellar absorption feature and constrain the dominant age of the nuclear stellar population to ~1 Gyr. Finally, we find regions across the nucleus of NGC 404 with [Fe II]/Paβ line ratios up to 6.5, ~2.5 times higher than the ratio measured from spatially integrated spectra. From these high line ratios, we conclude that shocks are the dominant physical mechanism exciting NGC 404's LINER emission and argue that a possible source of this shock excitation is a supernova remnant.

Key words: galaxies: active – galaxies: individual (NGC 404) – galaxies: nuclei – infrared: galaxies – techniques: imaging spectroscopy

Supporting material: data behind figure

1. Introduction

Low-ionization nuclear emission-line region (LINER) galaxies, first defined by Heckman (1980), are the least luminous but most common class of active galactic nucleus (AGN), with ~1/3 of all galaxies within 40 Mpc hosting LINER emission at their centers (Ho et al. 1997b). LINERs are identified by their optical emission-line properties and show high values of line ratios with low-ionization species (e.g., [N II]/Hα) similar to Seyferts but low values of line ratios from high-ionization species ([O III]/Hβ). These optical line ratios can be explained by a number of excitation mechanisms, with two dominant models being photoionization from a weakly accreting supermassive black hole (BH) or fast shock excitation (Riffel et al. 2013). Although the physical mechanisms exciting optical LINER emission likely vary across the class, studying LINERs in detail can reveal under what circumstances different excitation mechanisms dominate and help us determine the importance of BH accretion, feedback, and other physical processes such as star formation in the nuclei of relatively normal galaxies. The closest LINERs are ideal targets for detailed studies of individual nuclei because diffraction-limited angular resolutions of ~0″1 can probe physical scales of 5 pc,

allowing the excitation mechanisms in a single nucleus to be disentangled at very high spatial resolutions.

NGC 404 hosts one of the closest LINERs (Ho et al. 1997a) at a distance of only 3.1 Mpc away (Lee & Jang 2016) and is therefore an ideal source for studying the important physical processes at the centers of these galaxies. There is tentative evidence that NGC 404 hosts an accreting central BH from detections at X-ray (Binder et al. 2011) and radio (e.g., Nyland et al. 2012) wavelengths and variability observed at near-infrared (NIR), optical, and UV wavelengths (Maoz et al. 2005; Nguyen et al. 2017). A recent work attributed the radio source to a ratio jet launched by a central low-mass, low-Eddington-ratio BH (Nyland et al. 2017). NIR studies of the molecular gas and stellar dynamics in the nucleus of NGC 404 have placed an upper limit on the mass of this putative central BH of $1.5 \times 10^5 M_\odot$, in the mass range of an intermediate-mass BH (Seth et al. 2010; Nguyen et al. 2017). Despite evidence for the presence of an accreting central BH, it has been unclear whether photoionization from the BH accretion disk or another mechanism such as shock excitation is the dominant physical process in the NGC 404 nucleus driving its LINER emission.

NGC 404, and LINERs in general, also stand out from other emission-line galaxies in their NIR spectral properties. The NIR spectra of these nuclei in the J (1.1–1.4 μm) and K (2.0–2.4 μm) bands often show features from [Fe II], H$_2$, and the Paβ and Brγ hydrogen recombination lines. At the spatial resolutions of ~100 pc probed by previous seeing-limited slit spectroscopy observations, LINERs exhibit high ratios of [Fe II]/Paβ and H$_2$/Brγ compared to Seyfert and starburst

---

[6] Corresponding author.

nuclei (Larkin et al. 1998; Rodríguez-Ardila et al. 2004, 2005; Riffel et al. 2013). In particular, NGC 404 shows some of the highest values of these line ratios, with the [Fe II]/Paβ line ratio of 2.7 being similar to shocked regions of supernova remnants (Larkin et al. 1998). The [Fe II]/Paβ ratio is sensitive to shock excitation because iron is typically locked in dust grains, and high values of [Fe II]/Paβ (>2.0) require shocks that can destroy or ablate the dust and convert a sufficient amount of iron to a gaseous state (Blietz et al. 1994; Larkin et al. 1998). With the advent of adaptive optics (AO), the NIR diagnostic spectral features can be probed in LINERs at spatial resolutions 100 times smaller than seeing-limited observations using NIR integral field spectroscopy (IFS). These data consist of thousands of spectra taken simultaneously and can resolve differences in the [Fe II] and H_2 emission and kinematics on spatial scales of only 1 pc at the nearby distance of NGC 404, thereby spatially separating out regions in the nucleus of this galaxy that are dominated by shock excitation, star formation, and other physical processes. Using IFS data to spatially resolve differences in the [Fe II]/Paβ line ratio in particular can reveal regions of high [Fe II]/Paβ that are averaged out in seeing-limited spectra. LINERs in general have been included in past NIR IFS studies of nearby galactic nuclei (e.g., Mazzalay et al. 2013; Müller-Sánchez et al. 2013), but these studies focused on characterizing the molecular gas emission and the stellar absorption features in the K band and did not probe the shock-sensitive [Fe II] emission line in the J band.

We present results of NIR IFS observations of the nucleus of NGC 404 using the OSIRIS instrument at the W. M. Keck Observatory. These observations are a part of a larger survey of nearby LINER galaxies with the goal of constraining the excitation mechanisms of NIR emission lines at the highest possible spatial scales. We present data at both the J and K bands that measure the emission morphology, kinematics, and physical conditions of the ionized iron and molecular hydrogen gas at spatial scales of 1 pc. This work includes the first high spatial resolution study of the shock-sensitive [Fe II] line in NGC 404. Based on the spatially resolved spectral features and continuum emission, we find that the OSIRIS observations of the NGC 404 nucleus are best explained by at least four major physical components, including a nuclear stellar population, a central rotating H_2 disk, an H II region, and an extended shock front traced by strong [Fe II] emission. Section 2 describes the OSIRIS observations and data reduction procedures. Section 3 describes the data analysis and the resulting measurements of the stellar and ionized/molecular gas properties. Section 4 discusses the implications of these results on the stellar population and the physical mechanisms exciting the NIR emission in NGC 404.

2. Observations and Data Reduction

NGC 404 was observed on 2014 September 2 and 2015 October 8 using the OSIRIS instrument (Larkin et al. 2006) on the Keck I telescope. OSIRIS is an integral field spectrograph coupled to the Keck Adaptive Optics System (van Dam et al. 2006; Wizinowich et al. 2006). This instrument uses an array of small lenses to sample the AO image and produces up to ~3000 spectra simultaneously across a rectangular, contiguous field of view. The data were taken with the 50 mas (2014 September) and 35 mas (2015 October) plate scale modes using two different filters: Jn2 ($\lambda = 1.228$–$1.289\,\mu m$) and Kbb ($\lambda = 1.965$–$2.381\,\mu m$). The Jn2 filter covers the [Fe II] ($\lambda_0 = 1.2567\,\mu m$) and Paβ ($\lambda_0 = 1.28216\,\mu m$)

emission lines for low-redshift galaxies ($z < 0.004$). The Kbb filter covers a series of H_2 emission lines, including the 1–0 S(1) transition ($\lambda_0 = 2.1218\,\mu m$), as well as the Brγ line ($\lambda_0 = 2.16612\,\mu m$) and stellar absorption features, particularly the CO bandheads ($\lambda_0 = 2.29\,\mu m$). At the nearby distance of NGC 404, the angular pixel scales of 50 and 35 mas correspond to 0.8 and 0.5 pc, respectively. See Table 1 for a summary of the OSIRIS observations of NGC 404.

The on-source observations of NGC 404 total 0.75 hr in the 50 mas mode on 2014 September 2 and 1.25 hr in the 35 mas mode on 2015 October 8 in each filter, with individual frames having an integration time of 900 s. The airmass of NGC 404 during the observations ranged from 1.0 to 1.2. The data were taken using the Keck laser guide star AO system (van Dam et al. 2006; Wizinowich et al. 2006), with the bright, point-like nucleus of the galaxy serving as the tip/tilt reference source ($V_{mag} \approx 15$ within 0″5 González Delgado et al. 2008). The galaxy was dithered within the field of view such that previous or subsequent on-source frames could be used for sky subtraction, with typical dithers being 1″. In addition to the on-source frames, one 900 s pure-sky frame offset ~4″ from the source was taken in each filter and plate scale mode.

To correct for atmospheric absorption features, we also observed two telluric standard stars at an airmass similar to the science observations and with the same plate scale/filter setups: an A star (A0 star HD 13869 in 2014 and A1 star HD 217186 in 2015) and a G2 star (HD 12846 in 2014 and HD 217577 in 2015). Both the A and G star spectra were divided by a blackbody spectrum to remove the continuum shape of the stellar photosphere. The spectrum of the A star was used as the telluric spectrum across the majority of both observation bands, with the exception of the regions around the strong hydrogen absorption features of Brγ and Paβ. For these wavelength regions (1.270–1.289 μm in Jn2 and 2.156–2.177 μm in Kbb), the G2 spectrum was used, with the stellar absorption features removed by dividing the G2 spectrum by the solar spectrum. The solar spectrum used to correct the G2 star was created by the European Southern Observatory (ESO) using National Solar Observatory/ Kitt Peak Fourier Transform Spectrograph data produced by the NSF/NOAO.[7] Before dividing the OSIRIS G2 spectrum by the solar spectrum, the solar spectrum was shifted to match the radial velocity (RV) of the star and scaled so that the width of the hydrogen absorption line matched the G2 spectrum. Note that the value of the blackbody temperature used to correct for the shape of the stellar continuum emission affects the final telluric spectrum at a level of <1% for a wide range of temperatures (±2000 K). Finally, the resulting telluric spectrum was normalized to a median of 1.0 across all wavelengths, so that dividing by this spectrum corrects for the atmospheric absorption and instrumental throughput as a function of wavelength and does not change the overall level of the galaxy spectrum.

All the data were reduced using version 3.2 of the OSIRIS Data Reduction Pipeline (DRP; Krabbe et al. 2004). Each individual science frame was sky-subtracted by both the pure sky and its dithered pair frame (if applicable). The scaled-sky DRP routine was also performed on each frame. This routine scales the intensity of different families of OH lines in intensity to match the sky frame and science frame and is based on the algorithm developed by Davies (2007). All sky-subtracted frames were visually compared, and the frame with the lowest

---

[7] http://www.eso.org/sci/facilities/paranal/decommissioned/isaac/tools/spectroscopic_standards.html
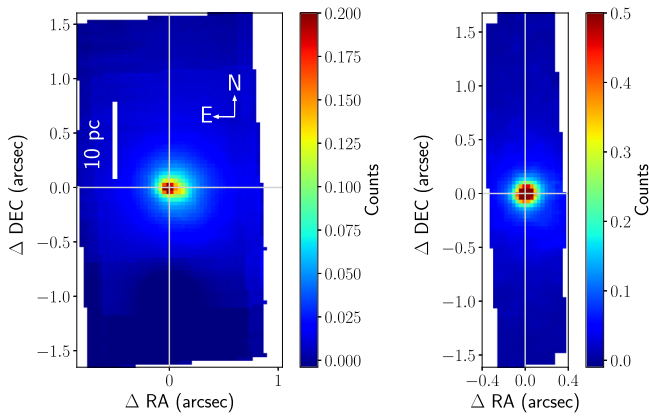
Figure 1. The NGC 404 reduced and telluric-corrected data cubes from the Jn2 band (left) and the Kbb band (right) collapsed along the wavelength axis. The displayed maps were made by taking the average value of the spectrum in each spaxel across the entire wavelength range in each band and are thus dominated by that band's continuum emission. The origins of these and all subsequent plots are set to the central peak of the Jn2/Kbb continuum emission as determined by a two-dimensional Gaussian fit to the emission in each collapsed data cube (also indicated by the gray crosshairs). We find that the nuclear *J*- and *K*-band continuum emission is compact and point-like. The data used to create this figure are available.

OH line residuals was chosen as the final sky-subtracted frame. These sky-subtracted frames were then mosaicked to create the final data cube for each filter. These final cubes have a wavelength sampling of $0.00015 \, \mu m$ in the Jn2 band and $0.00025 \, \mu m$ in the Kbb band, corresponding to a velocity resolution of $\sim 35 \, \mathrm{km \, s^{-1}}$ in both bands. The reduced data cubes were also wavelength calibrated by the DRP using information from arc lamp calibration data and OH sky lines. Finally, the spectrum of each spatial pixel, or spaxel, in the mosaicked cube was divided by the telluric spectrum created from the A and G star spectra. All subsequent data analysis was performed on these telluric-corrected data cubes. The units of the final spectra in each wavelength channel as reduced by the DRP are counts, which are proportional to the flux density of the galaxy.

Figure 1 shows the final Jn2 and Kbb 35 mas data cubes of NGC 404 averaged across all wavelengths in the filter, and Figure 2 shows an example spectrum extracted from each of these data cubes. The peaks of the Jn2 and Kbb continuum emission as determined by a two-dimensional Gaussian fit to the spectrally averaged data cubes were used to spatially register the two data sets to each other. We find that the continuum emission is point-like in the OSIRIS data and has an average FWHM of $0\rlap{.}''16$ and $0\rlap{.}''13$, respectively; however, it is difficult to determine whether it is a true point source or slightly resolved because the core of the galaxy was used as the tip/tilt star. Since the 35 mas data from 2015 October 8 are deeper and have a finer spatial sampling, analyses derived from these data are presented in subsequent sections of this work unless otherwise noted.

The instrumental dispersion and its variation across the mosaicked field of view were estimated by measuring the widths of OH sky lines in different apertures. A set of four apertures was chosen for each filter to fall in the sky regions separated from the continuum emission of the galaxy nucleus. In the Jn2 band, the four apertures are offset from the continuum center by $\pm 0\rlap{.}''5$ in the *x* (east/west) direction and $\pm 0\rlap{.}''67$ in the *y* (north/south) direction. In the Kbb band, the
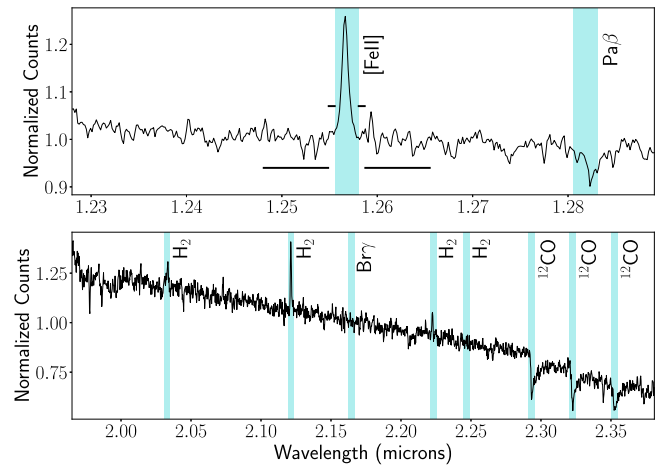

Figure 2. Spectrum of the nucleus of NGC 404 in the Jn2 (top) and Kbb (bottom) bands. The vertical bars indicate the wavelengths of the various spectral features at the systemic velocity of NGC 404 ($-48 \, \mathrm{km \, s^{-1}}$) and span a $\pm 300 \, \mathrm{km \, s^{-1}}$ velocity range around the central wavelength. Horizontal lines indicate the spectral ranges used to determine the continuum (shown above the spectrum) and noise (shown below) for the [Fe II] line (see Section 3.1). Each spectrum was extracted from the Jn2/Kbb data cubes using an aperture centered on the continuum peak with a radius of 5 spaxels, or 2.6 pc. The spectra show emission from the [Fe II] line in the Jn2 band and multiple H_2 lines in the Kbb band. Stellar absorption features from Paβ and the ^{12}CO bandheads are also visible. Although not detected in this central aperture, Paβ and Brγ are also seen in emission to the north of the NGC 404 nucleus (see Figure 3).

four aperture locations have the same *x* value as the continuum center and are offset in the *y* direction by ± 1.33 and $\pm 0\rlap{.}''67$. The OH line widths in each aperture were estimated by Gaussian fits to three emission lines. In the Jn2 band, the chosen OH lines are close in wavelength, so their line profiles are fit simultaneously with a model consisting of a sum of three Gaussians. The continuum in these spectra was estimated separately by performing a parabolic fit to the majority of the spectrum, with the exact wavelength range adjusted to give a good estimate of the wavelength range of the OH lines on the red side of the bandpass. In the Kbb band, the OH lines are well separated, so the line is fit individually, and the continuum was modeled by adding a delta offset to the Gaussian line profile model. The median values of the Jn2 and Kbb σ values for the OH lines are 0.21 and 0.25 nm, respectively. These instrumental line widths are equivalent to velocity dispersions of $50 \, \mathrm{km \, s^{-1}}$ in the Jn2 band and $35 \, \mathrm{km \, s^{-1}}$ in the Kbb band.

3. Data Analysis and Results

3.1. Line Emission S/N Estimate

The signal-to-noise ratios (S/Ns) for the [Fe II] and 1–0 S(1) H_2 emission lines were computed for every spaxel in the mosaicked data cubes for use in subsequent analysis steps. The continuum for this calculation was taken as the average of counts in the wavelength channels from -450 to $-300 \, \mathrm{km \, s^{-1}}$ and from $+300$ to $+450 \, \mathrm{km \, s^{-1}}$ relative to the systemic velocity. The noise was estimated by taking the standard deviation of 10 wavelength channels on either side of the line, starting at $\pm 300 \, \mathrm{km \, s^{-1}}$ and moving outward. Every fifth wavelength channel was used for the noise estimate to avoid the correlated noise present in adjacent wavelength channels.

Signal and noise maps were created for the [Fe II] and 1–0 S(1) H_2 emission lines by computing the signal and noise for each

emission line in each spaxel. Due to the noise present in the signal and noise estimates, the signal and noise maps were then smoothed using a 2D Gaussian with a σ of 3.5 pixels in both the x and y directions. This smoothing was implemented using the `Gaussian_filter` function in the `ndimage` module of the SciPy library, a scientific computing library for the Python programming language. The ratio of these smoothed maps was then used as the spatial map of the S/Ns for each of the [Fe II] and 1–0 S(1) H_2 emission lines in subsequent analysis steps. The values of the smoothed S/N maps range from zero in locations where there is no detected line flux to 25 in the spaxels with the maximum line flux.

3.2. Velocity-integrated Emission-line Flux Maps

Spatial maps of the continuum-subtracted emission-line fluxes of the [Fe II], Paβ, 1–0 S(1) H_2, and Brγ lines were constructed to compare the morphology of the different lines. The emission-line flux in each individual spaxel was found by summing the continuum-subtracted counts in seven wavelength channels (a velocity range of approximately $\pm100\,\mathrm{km\,s^{-1}}$) centered on the emission-line wavelength. This velocity range was chosen to capture the majority of the line emission while still excluding channels without emission that would only add noise to the line-flux measurement. For the [Fe II] and 1–0 S(1) H_2 emission lines, velocity information was used to determine the emission-line wavelength in spectra with an emission-line S/N greater than 10 (see Section 3.1). For spaxels with a line S/N less than 10, the emission-line wavelength was set as the vacuum wavelength of the line shifted to the systemic velocity of the galaxy. For the Paβ and Brγ emission lines, the systemic velocity of the galaxy was used to determine the emission-line wavelength in every spaxel, since these lines are detected with high significance in only a few spatial locations. The continuum around each line was estimated using the average of counts in the wavelength channels from -450 to $-300\,\mathrm{km\,s^{-1}}$ and from $+300$ to $+450\,\mathrm{km\,s^{-1}}$ relative to the systemic velocity of the galaxy.

The resulting emission-line flux maps for four emission lines are shown in Figure 3. We find that the morphologies of the [Fe II], H_2, and Paβ/Brγ lines vary at the pc spatial scales probed by these data. The [Fe II] emission is diffuse and extended out to $\sim0\farcs5$ (8 pc) from the nucleus of NGC 404, while the H_2 is more spatially compact. The majority of the H_2 emission is contained in a central peak coincident with the continuum center of the K-band emission, with weaker H_2 emission visible to the southeast of the nucleus. The Paβ and Brγ are seen both in absorption at the nucleus and in emission $\sim0\farcs2$ (3 pc) north of the nucleus of NGC 404.

3.3. Velocity-resolved Emission-line Flux Maps

The emission morphology of each line can also be viewed as a function of velocity to reveal morphological structures that only appear at specific velocities. First, continuum-subtracted line cubes for each emission line were created by selecting a subset of wavelength channels around the emission line and then estimating and subtracting a continuum value for every spatial pixel. The continuum value was determined using the same method as for the velocity-integrated line maps, by taking the average of the counts in wavelength channels from -450 to $-300\,\mathrm{km\,s^{-1}}$ and from $+300$ to $+450\,\mathrm{km\,s^{-1}}$. The wavelength ranges of the line cubes were chosen to span at least
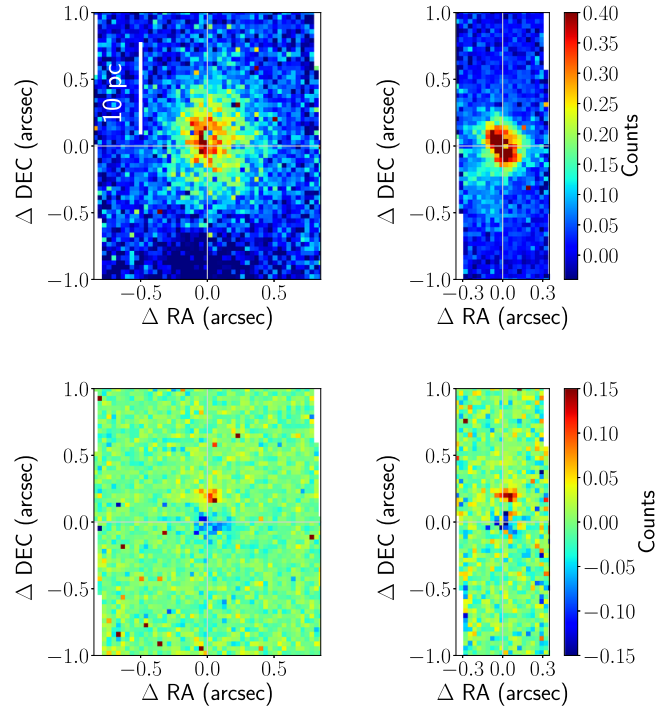

Figure 3. Velocity-integrated emission-line flux maps across the central 20 pc of NGC 404 for four emission lines: [Fe II] (top left), 1–0 S(1) H_2 (top right), Paβ (bottom left), and Brγ (bottom right). The [Fe II] and Paβ maps were derived from the Jn2 data, and the H_2 and Brγ maps were derived from the Kbb data. These line maps are the sum of the continuum-subtracted emission in wavelength channels approximately $\pm100\,\mathrm{km\,s^{-1}}$ around the line relative to the systemic velocity of NGC 404. The displayed maps are subsets of the full field of view of the mosaicked data cubes shown in Figure 1 ($1.65 \times 3\farcs29$ in the Jn2 band and 0.70×3.33 in the Kbb band) and show the regions in which line emission is detected. The [Fe II] emission is diffuse and extended out to $\sim0\farcs5$ (8 pc) from the nucleus of NGC 404. The bulk of the H_2 emission is more compact, with additional regions of emission to the bottom left of the nucleus. The Paβ and Brγ lines are seen in absorption at the nucleus (blue) and in emission $\sim0\farcs2$ (3 pc) north of the nucleus (red).

$\pm300\,\mathrm{km\,s^{-1}}$ around the lines relative to the systemic velocity of the galaxy to fully cover the wings of each emission line. The wavelength channels of each line cube were then resampled to velocities from -250 to $250\,\mathrm{km\,s^{-1}}$ with a spacing of $25\,\mathrm{km\,s^{-1}}$. This resampled spacing is slightly smaller compared to the native wavelength channel spacing of the OSIRIS data cubes ($\sim35\,\mathrm{km\,s^{-1}}$ in both the Jn2 and Kbb bands). The final emission-line flux maps at each velocity were then made by taking the average of the channel at the given velocity and the two channels on either side ($\pm25\,\mathrm{km\,s^{-1}}$) in the resampled line cubes.

Figure 4 shows the resulting velocity-resolved line-flux maps for the [Fe II], Paβ, 1–0 S(1) H_2, and Brγ emission lines. The [Fe II] emission shows a complex velocity structure, with the brightest and most extended emission at 0 and $50\,\mathrm{km\,s^{-1}}$. Low surface brightness [Fe II] emission extends out to high velocities from -150 to $+200\,\mathrm{km\,s^{-1}}$. At -50 and $0\,\mathrm{km\,s^{-1}}$, the shape of the [Fe II] emission extends to the north and southwest of the nucleus. This extended structure is coincident with an arc-like feature visible at these velocities in the 50 mas data set shown in Figure 14. The H_2 emission is more spatially compact than the [Fe II] emission and spans a smaller overall velocity range of $\pm100\,\mathrm{km\,s^{-1}}$. The emission peaks in the $0\,\mathrm{km\,s^{-1}}$ channel where it aligns with the continuum center of the Kbb emission. The $\pm50\,\mathrm{km\,s^{-1}}$ H_2 emission is offset from
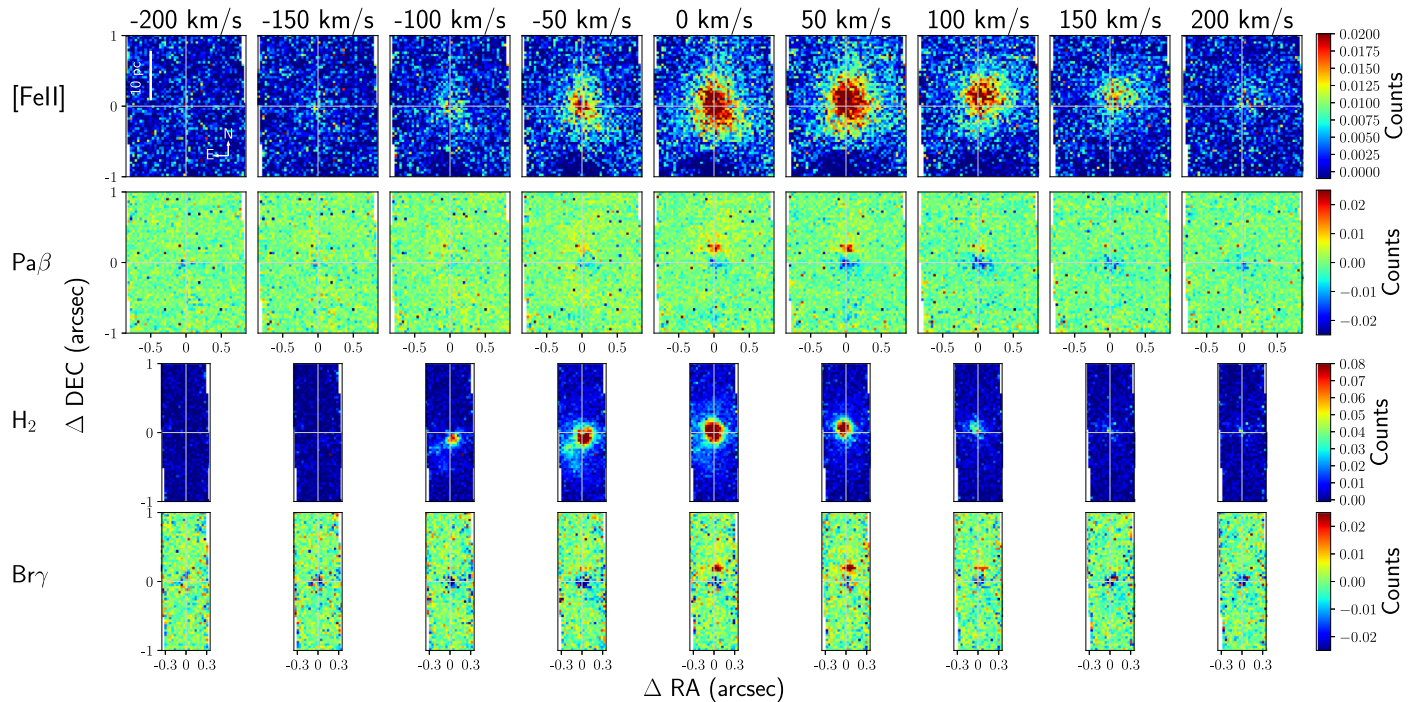
Figure 4. Velocity-resolved emission-line maps for emission lines [Fe II], Paβ, 1–0 S(1) H$_2$, and Brγ. The displayed velocity is relative to the systemic velocity of the galaxy. The crosshairs indicate the continuum center of the galaxy in the Jn2 ([Fe II], Paβ) or Kbb (H$_2$, Brγ) bands. These maps show that the [Fe II] emission is extended and diffuse compared to the compact H$_2$ and Paβ/Brγ emission and spans the largest velocity range of all the emission lines (-150 to $+200$ km s^{-1}). At -50 and 0 km s^{-1}, the [Fe II] emission is extended to the north and southwest of the nucleus, coincident with the arc-like structure seen in the 50 mas data (see Figure 14). The central peak of the H$_2$ emission shifts position from the southwest of the continuum center to the northeast with increasing velocity, a signature of rotational motion. Two additional blueshifted knots of H$_2$ emission to the southeast of the nucleus are visible in the -50 and 0 km s^{-1} maps.

the continuum center to the southwest and northeast, respectively, showing that two sides of the central molecular gas emission have different velocities, which is similar to what is expected from a rotating disk with a position angle of its rotation axis equal to about $-45°$ on the plane of the sky. The two knots of H$_2$ emission offset from the continuum center to the southeast are brightest in the -50 km s^{-1} map, revealing their blueshifted velocity offset from the central region of molecular emission. These blueshifted H$_2$ structures are not matched in the [Fe II], Paβ, or Brγ emission lines. The Paβ and Brγ maps show similar morphologies to each other across all velocity channels. The knot of emission north of the nucleus seen in these lines spans from -50 to 100 km s^{-1}, with the brightest emission found at 0 and 50 km s^{-1}. The velocities of the brightest Paβ/Brγ emission match that of the brightest [Fe II] emission. Additionally, this bright emission region is spatially located where the [Fe II] emission is also very strong. The Paβ and Brγ are also seen in absorption at the center of the NGC 404 nucleus, which can be used to constrain the stellar population in this central region.

3.4. Emission-line Kinematics: [Fe II] and H$_2$

The velocity shifts of [Fe II] and the 1–0 S(1) H$_2$ emission lines in a given spectrum were estimated using a Gaussian fit to the line profiles. The fits were performed in a wavelength range of $\sim$0.003 μm around the vacuum wavelength of the emission lines. This wavelength range corresponds to approximately ± 350 km s^{-1} in the Jn2 band and ± 200 km s^{-1} in the Kbb band. The model parameters include the central wavelength, σ, and integrated flux of the Gaussian emission line, as well as a vertical offset to model the continuum in the region around the

line. The central wavelength and σ of the best-fit Gaussian were converted into the velocity and velocity dispersion of the emission line. These fits were performed on each individual spectrum and on spatially binned spectra in square bins that are 2 spaxels (70 mas) on a side. These binned spectra were created by taking the median of the four individual spectra in each bin.

The velocity and velocity dispersion maps for the [Fe II] and 1–0 S(1) H$_2$ emission lines are displayed in Figure 5. The velocity is displayed for each individual spaxel, while the velocity dispersion is displayed for the spatially binned spectra to reduce noise. To create the displayed dispersion maps, the instrumental dispersion determined in Section 2 for each observing band was subtracted in quadrature from the measured velocity dispersion. For the $\sim$5 bins with measured velocity dispersions less than the instrumental dispersion, the dispersion is set to zero in Figure 5 for display purposes. Individual spaxels with an S/N less than 10 in the smoothed S/N maps are masked. Additionally, spaxels whose Gaussian fit does not converge or whose best-fit velocity falls outside the wavelength range are also masked. The same mask was applied to both the velocity and the velocity dispersion maps.

The [Fe II] and H$_2$ gases show very different velocity structures. The H$_2$ velocity map is consistent with simple rotation centered on the nucleus of NGC 404 with a velocity shift of ± 30 km s^{-1} across the central $\sim$15 pc of the galaxy. The two peaks of H$_2$ emission offset to the southeast of the nucleus are found to be blueshifted by $\sim$30 km s^{-1} relative to the systemic velocity of the galaxy. The [Fe II] velocity gradient is roughly perpendicular to the gradient of the molecular gas and spans a larger range of velocities, with the northwest region of emission having velocities up to 80 km s^{-1} relative to the systemic velocity of the galaxy. This region with
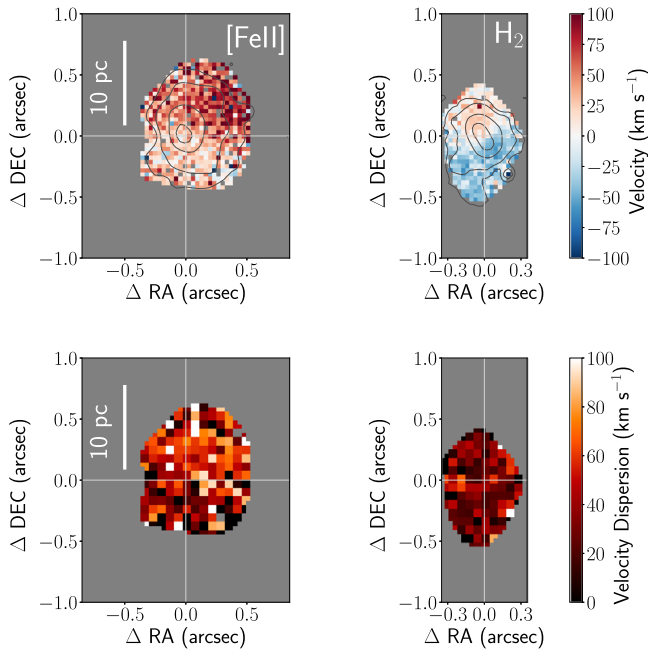
Figure 5. Velocity (top row) and velocity dispersion (bottom row) for the [Fe II] (left column) and 1–0 S(1) H_2 (right column) emission lines. The velocity maps are shown for every individual spaxel, and the velocity dispersion maps are shown for spectra in spatial bins measuring 2×2 spaxels (70 mas). Contours showing the morphology of the [Fe II] and 1–0 S(1) H_2 emission as displayed in Figure 3 are overplotted in dark gray. The velocities are shown relative to the systemic velocity of NGC 404 and with the red colors indicating redshifts and the blue colors indicating blueshifts. The instrumental dispersions were subtracted from the measured velocity dispersions to yield the displayed dispersion maps. Individual spaxels with a line S/N of less than 10 are masked. Spaxels whose Gaussian line fit did not converge or whose best-fit velocity falls outside the fitting range are also masked. We find that [Fe II] and H_2 show different kinematics with velocity gradients that are roughly perpendicular to each other. The [Fe II] line reaches high velocities up to 80 km s^{-1} and has a higher dispersion than the molecular gas. The velocities of the central H_2 emission are dominated by rotational motion with a velocity gradient of ± 30 km s^{-1}. The two knots of H_2 emission to the southeast of the nucleus are blueshifted by ~ 30 km s^{-1}.

the highest [Fe II] velocities also shows higher velocity dispersion, with values up to 75 km s^{-1}. The H_2 gas shows no spatial variation of the velocity dispersion and has generally lower dispersion than the [Fe II] gas.

3.5. Absorption-line Kinematics: CO Bandhead

The CO bandhead is a set of strong absorption features primarily from the atmospheres of giant stars. With resolved spectroscopy, this stellar absorption feature can be used to track the kinematics of the stars in the center of NGC 404. We measured the velocity shift of the CO bandhead absorption feature in each individual spectrum relative to the spectrum of the spaxel that has the brightest Kbb continuum. The velocity shift between a spectrum in a single spaxel and the reference spectrum was found by cross correlating the two spectra in the wavelength region containing the CO bandhead features (2.27–2.365 μm). The peak of the resulting cross-correlation was then found by fitting a Gaussian to the cross-correlation function. Note that the stellar kinematics that we measure are therefore all relative to the velocity of this reference spectrum and are not absolute velocities like those we measure for the gas kinematics.
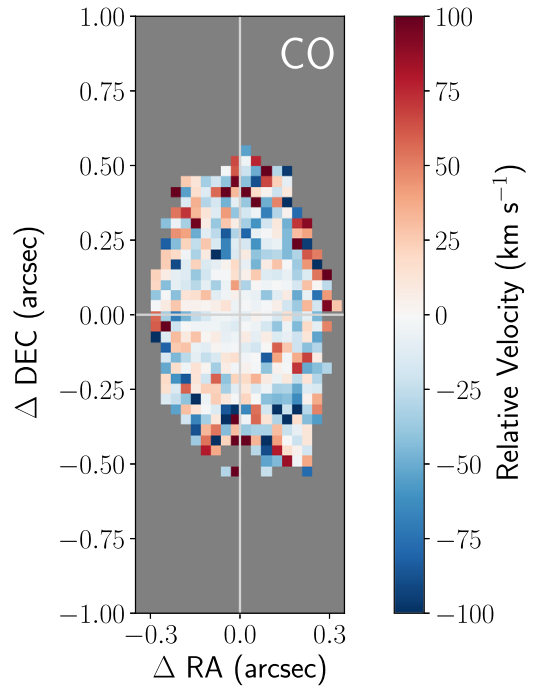

Figure 6. Relative stellar velocity map as measured by the CO bandhead absorption feature. The stellar velocities are displayed only for individual spaxels with continuum S/N greater than 7.0. The velocity shifts were measured relative to the spaxel with the highest Kbb continuum emission, which is the spaxel at the origin of this plot. The color bar used here matches the color bar used in Figure 5 for the [Fe II] and H_2 gas kinematics. The CO velocity shows no significant variation across the central ~ 15 pc of NGC 404 in contrast with the [Fe II] and H_2 emission lines, thus revealing that the stars are not moving at the same velocities as the gas.

The resulting stellar velocity map is shown in Figure 6. Only spaxels with a continuum S/N greater than 7.0 are displayed. This continuum S/N was computed using the DER_SNR algorithm, which is a simple and robust algorithm that uses the entire spectral range to compute both the signal and the noise and accounts for correlated noise between neighboring wavelength channels (Stoehr et al. 2008). We find no significant variation in the stellar velocity within the central ~ 15 pc of NGC 404.

To confirm the lack of stellar velocity gradient in the data and compare to the ionized and molecular gas velocities, we also measured the stellar velocity in apertures that have large differences in gas velocities. Circular apertures with radii of 4 pixels (2 pc) were placed on five locations with high/low [Fe II] or 1–0 S(1) H_2 velocities. These apertures are over-plotted on the [Fe II] and 1–0 S(1) velocity maps, and the spectra extracted from each aperture are shown in Figure 7. Pairs of CO spectra with high/low [Fe II] or H_2 velocities were also cross-correlated with each other to check for stellar velocity shifts. We find that there is no stellar velocity shift visual in the extracted spectra and measure relative velocities of -20 ± 14, 0 ± 10, and 2 ± 12 km s^{-1} from the spectra in apertures 1 and 2, 3 and 4, and 3 and 5, respectively. The errors were determined by the standard deviation of the velocity shifts measured from each of the three individual CO bandheads in the spectra. These stellar velocity shifts from the CO bandhead spectra are consistent with 0 km s^{-1}, and we therefore find that the stellar velocity field is distinct from both the ionized and molecular gas kinematics.
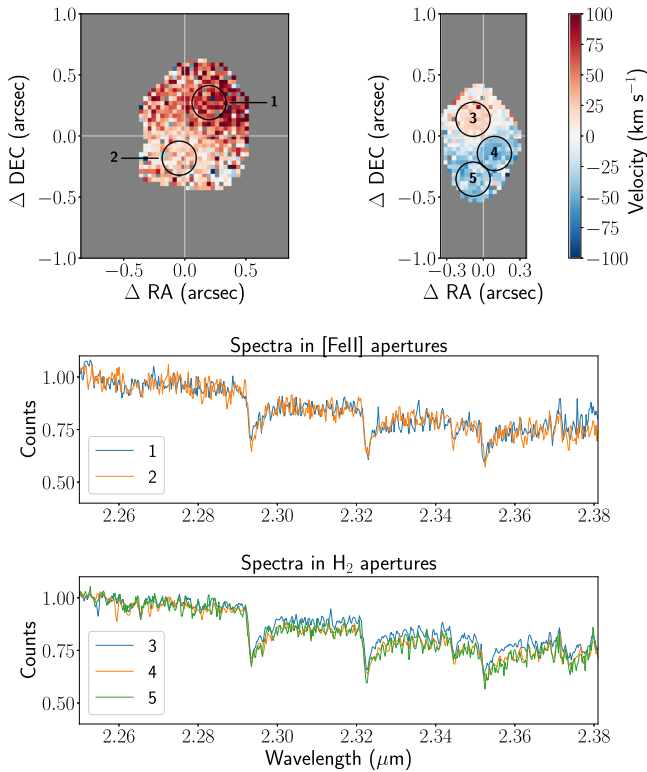
Figure 7. Comparison of CO bandhead absorption features in five spatial apertures centered on regions of high/low [Fe II] or 1–0 S(1) H_2 velocities to confirm that the stellar velocity is constant even in regions with large gradients in ionized/molecular gas velocity. The five circular apertures used are overplotted on the [Fe II] and H_2 velocity maps in the top two panels. The lower two panels display the five spectra extracted from these spatial apertures in the wavelength region around the CO bandhead spectral features. The spectra are separated into two groups: the two apertures centered on regions of high and low [Fe II] velocities and the three apertures centered on regions of high and low H_2 velocity. No stellar velocity shift is visible within these two groups of spectra, indicating that the stars are not moving in the same velocity field as either the ionized or molecular gas. Additionally, cross-correlation measurements between spectra within these groups also give stellar velocity shifts consistent with 0 km s^{-1}.

3.6. Molecular Hydrogen Line Ratios

We estimated the flux of multiple molecular hydrogen lines within the wavelength range of the K broadband filter. Combinations of these line fluxes can be used to estimate the rotational and vibrational excitation temperature of the H_2 and distinguish between different excitation mechanisms of this molecular gas. In addition to the strongest 1–0 S(1) line of H_2 in the NGC 404 spectra discussed above, there are three detected H_2 lines in the Kbb bandpass: 1–0 S(0) ($\lambda_0 = 2.2235\ \mu$m), 1–0 S(2) ($\lambda_0 = 2.0338\ \mu$m), and 2–1 S(1) ($\lambda_0 = 2.2477\ \mu$m). We estimated these four line fluxes in three different circular apertures with radii of 4 pixels = 0″.14. These apertures are centered on the different spatial structures observed in the 1–0 S(1) line map: the bright H_2 emission centered on the nucleus and the two weaker peaks of H_2 emission offset to the southeast of the nucleus. Figure 8 shows the apertures superimposed on this line-emission map and the corresponding extracted spectra. The continuum was estimated globally in each of the three spectra using a line fit to a large subset of the wavelength range: 2.02–2.28 μm. This range excludes regions on the blue side of the spectra that suffer from poor telluric correction and regions on the red side that contain

the CO bandhead absorption features while still covering the wavelengths of all four H_2 lines.

The H_2 line fluxes were then estimated from the continuum-subtracted spectra. First, the overall molecular hydrogen velocity in each aperture was estimated using the 1–0 S(1) line and the same Gaussian fitting method used for the individual spaxel velocity estimate (see Section 3.4). The 1–0 S(1) velocities relative to the systemic velocity of NGC 404 in the apertures from north to south are -5 ± 3, 39 ± 2, and 38 ± 3 km s^{-1}, respectively, where the error bars correspond to the fitting errors given by the curve_fit algorithm from the optimize module of the SciPy library. The flux of each line was then estimated by summing over wavelength channels with velocity in the range of ± 125 km s^{-1} relative to the 1–0 S(1) velocity of each aperture. This velocity range was chosen using the 1–0 S(1) line in the central aperture by estimating its flux with a variety of velocity ranges and finding the minimum range that captured all of the line flux.

The errors on the line fluxes in each aperture spectrum were estimated by applying the line-flux measurement method described above to areas of the spectrum with no line flux. Wavelength values were sampled from a uniform distribution across the continuum fitting range of 2.02–2.28 μm. Various spectral regions within this wavelength range were masked out, including around the four H_2 lines, the doublet absorption features from Na I (2.206/2.209 μm) and Ca I (2.263/2.266 μm), and strong OH sky lines. The 675 wavelength values remaining after the mask was applied were then used as the central wavelength for line-flux measurements. The standard deviation of these resulting simulated line-flux measurements was taken as the error on the measured H_2 line fluxes for each spectrum. For H_2 lines with fluxes that are less than 3σ above the error, a 3σ upper limit on the flux was determined using the method described in Section 3.7. The velocity dispersion of the Gaussian line profile that sets the limiting flux was taken as 50 km s^{-1} to match the measured dispersion of the 1–0 S(1) line, which is detected with high significance in all three apertures.

The line-flux measurements and errors for each aperture are presented in Table 2. This table also gives the H_2 line ratios 1–0 S(2)/1–0 S(0) and 2–1 S(1)/1–0 S(1) for each aperture. These line ratios are sensitive to the excitation mechanism of the molecular gas and derived using fluxes from both ortho (odd J) or both para (even J) hydrogen molecules, so that a ortho/para ratio does not need to be independently assumed. The 2–1 S(1) line is not detected above 3σ in apertures 1 and 2, so the upper limits on the line flux and the corresponding line ratio are reported. The other emission lines were detected above 3σ in all apertures and with the highest significance in aperture 2, where the lower underlying continuum emission relative to the H_2 line emission leads to a lower line-flux error. We find that both the 1–0 S(2)/1–0 S(0) and 2–1 S(1)/1–0 S(1) line ratios are consistent among all three spatial locations.

The H_2 line ratios measured here use pairs of emission lines that are far apart in wavelength and can therefore be affected by variations in Strehl ratio across the Kbb band. To quantify the effect of Strehl ratio variation across the H_2 line wavelengths, we divided the telluric-corrected Kbb data cube by a blackbody spectrum normalized to a median of 1.0 to remove the shape of NGC 404's continuum emission, so that any remaining variations in the aperture spectra are only due to variations in the Strehl ratio. A temperature of 4925 K was chosen to match
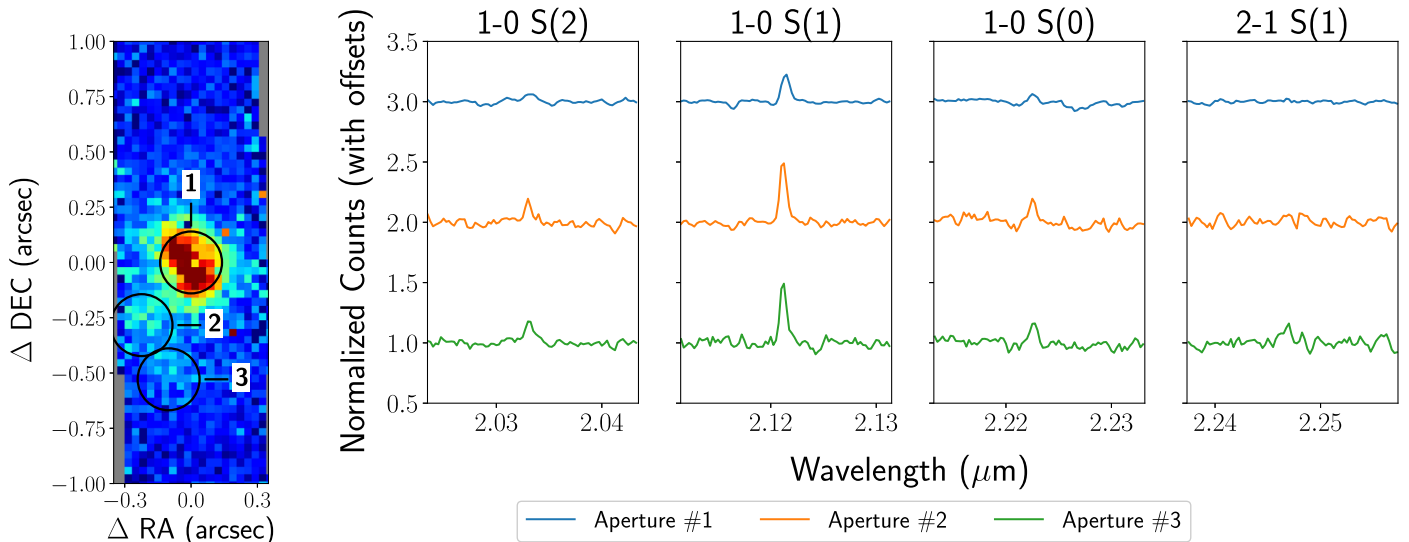
Figure 8. Left: 1–0 S(1) H$_2$ emission-line map with three apertures superimposed. The apertures each have a radius of 4 pixels = 0″.14 and were chosen to align with morphological features in the 1–0 S(1) emission map. Right: Kbb spectra extracted from the three apertures in the wavelength regions around the detected H$_2$ emission lines. These spectra were normalized to have a median of 1.0, and then an offset was applied for display purposes. The wavelength regions around each H$_2$ line are plotted in separate panels. The 1–0 S(2), 1–0 S(1), and 1–0 S(0) H$_2$ lines are detected in all three apertures, and the 2–1 S(1) line is only detected in aperture 3.

the F547M − F814W (roughly V − I) color of ∼0.95 measured in the unreddened region of the galaxy's nucleus using the *Hubble Space Telescope* (*HST*; see Section 3.1 of Seth et al. 2010 and note that adjusting the temperature by ±1000 K affects the blackbody spectrum shape by <1% across the Kbb band). We compared the median value of the divided aperture spectra in regions ±0.01 μm around the H$_2$ lines of interest and find that the Strehl ratio variations affect the line ratios at a level of 0.5%–7% across the two line ratios and the three apertures. The 25%–35% statistical error on the line ratios reported in Table 2 therefore dominates the error budget, and the measured line ratios are not significantly affected by Strehl ratio variation in our data.

3.7. [Fe II]/Paβ and H$_2$/Brγ Line Ratios

The line ratios of [Fe II]/Paβ and 1–0 S(1) H$_2$/Brγ were measured to constrain the excitation mechanisms at different physical locations at the center of NGC 404. In general, the S/N of the hydrogen recombination lines is not high enough to estimate their line flux in any but a few spaxels (see Figure 3), so these line ratios were instead measured in various circular apertures placed within the shared Jn2/Kbb FOV with radii ranging from 2 to 4 pixels (1–2 pc). We defined these apertures by starting with the three apertures used for the H$_2$ line ratio measurements in Section 3.6, which are centered on the NGC 404 nucleus and two other areas of H$_2$ emission. An additional aperture was applied to the location of the Paβ/Brγ emission peak to the north of the nucleus. Other apertures were then added to cover the full spatial extent of the [Fe II] line, the most spatially extended emission line. The radii of these apertures are between 2 and 4 pixels, depending on the S/N. Figure 9 displays the final set of apertures overplotted on all four line-emission maps.

In the Jn2 filter, the bandpass is so narrow that a global continuum fit is difficult to perform consistently for all aperture spectra. Instead, a local continuum around each line was estimated by taking an average of the counts in wavelength channels on either side of the emission line. This method was

applied to both the Jn2 and Kbb data to maintain consistency between the bands. The default channels used for the local continuum calculation are −450 to −300 km s^{-1} and +300 to +450 km s^{-1}, the same velocity range used for the line S/N estimation described in Section 3.1. The flux of each line was then determined by summing the continuum-subtracted counts in wavelength channels containing the emission line, by default ±250 km s^{-1} relative to the systemic velocity of the galaxy. This velocity range was chosen to cover the wings of all four emission lines, including the cases in which the lines are Doppler shifted with respect to each other or the systemic velocity. In each aperture, the same continuum and line-flux velocity ranges were used for all four emission lines so that the [Fe II]/Paβ and H$_2$/Brγ line ratios are calculated using consistently measured line fluxes and can therefore be compared to each other.

If an emission line was not detected in an aperture, then an upper limit was placed on its line flux. This upper limit was only needed for the hydrogen recombination lines, since these lines have much lower S/N than the [Fe II] and 1–0 S(1) H$_2$ lines. An upper limit on the Paβ and Brγ lines corresponds to a lower limit on the [Fe II]/Paβ and H$_2$/Brγ line ratios. A conservative 3σ upper limit was calculated by taking the flux from a Gaussian emission line with a peak of three times the noise estimate described in Section 3.1 and a velocity dispersion of 100 km s^{-1}. This dispersion value is on the high end of the observed velocity dispersions of the [Fe II] and H$_2$ emission lines (see Figure 5), giving a conservative upper limit for the line flux. The flux of the Gaussian was computed by sampling the Gaussian at wavelength channels within the ±250 km s^{-1} velocity range and taking the sum of these values.

Table 3 gives the locations and radii of all 15 apertures, the velocity ranges used for the continuum and line-flux estimation, and the resulting line ratio measurements or lower limits. We find that [Fe II] and 1–0 S(1) H$_2$ lines are detected in all 15 apertures and Paβ and Brγ are detected in nine and three apertures, respectively. The lowest values of both line ratios ([Fe II]/Paβ = 2.5 and H$_2$/Brγ = 1.2) are found in the aperture centered on the peak of the Paβ and Brγ emission.

Table 1
Summary of OSIRIS Observations of NGC 404

Date	Filter	Wavelengths (μm)	Plate Scale (mas)	No. of Frames	Integration Time (hr)	FOV (arcsec) Single Frame	Mosaic
2014 September 2	Jn2	1.228–1.289	50	3	0.75	2.1×3.2	2.1×3.2
2014 September 2	Kbb	1.965–2.381	50	3	0.75	0.8×3.2	0.8×3.2
2015 October 8	Jn2	1.228–1.289	35	5	1.25	1.47×2.24	1.65×3.29
2015 October 8	Kbb	1.965–2.381	35	5	1.25	0.56×2.24	0.70×3.33

Six of the other apertures with Paβ detections are located to the north of the nucleus and show [Fe II]/Paβ ratios between 5.3 and 6.5. Two other apertures to the south of the nucleus also have Paβ detections with slightly lower values of 3.8 and 4.3, though these detections have lower S/N than the northern apertures. Two of the northern apertures also have detections of Brγ and show H$_2$/Brγ ratios of 2.4 and 2.7.

Additionally, there are six apertures in which Paβ absorption is detected, and for these apertures, no line ratio measurement or upper limit is reported. The Paβ absorption is accompanied either by very weak to no emission (apertures 1 and 12) or by strong emission (apertures 2, 11, 13, and 14). Figure 10 displays five representative spectra to show the variation seen within the center of NGC 404. The example spectra are an aperture centered on the nucleus of NGC 404 showing Paβ absorption and no emission (1), a northern aperture with both Paβ and Brγ detections (7), an aperture centered on the Paβ/Brγ emission (9), an aperture with simultaneous detection of Paβ absorption and strong emission (11), and a southern aperture with Paβ detected (15).

4. Discussion

The analysis and results in the previous section show that the five dominant spectral features (infrared continuum, hydrogen recombination lines, molecular hydrogen rotation-vibrational lines, CO bandhead absorption, and the [Fe II] emission line) all have distinct spatial and spectral structures and imply a complex nuclear environment within NGC 404. Indeed, the hydrogen recombination lines alone show areas of both emission and net absorption. In this section, we interpret the spectral properties of these five features in order to constrain the physical environment in the nucleus of NGC 404. In particular, we discuss constraints on the nuclear stellar population (Section 4.1) and the possible physical mechanisms responsible for exciting the H$_2$ (Section 4.2) and the [Fe II] gas emission (Section 4.3).

4.1. Stellar Population Constraints: CO and Paβ Absorption and Paβ Emission

The stellar population in the nucleus of NGC 404 contributes both to the infrared continuum and to the CO and hydrogen recombination absorption features measured in the OSIRIS observations of NGC 404. The infrared continuum observed at both the J band and the K band is centrally peaked, as shown in Figure 1. This continuum emission likely arises from a nuclear stellar population that is centered at this peak of continuum emission, which also coincides with the peak of the CO bandhead and Paβ/Brγ absorption. A nuclear star cluster was identified in NGC 404 by Ravindranath et al. (2001), and its stellar population has been been studied at optical wavelengths (Seth et al. 2010; Nguyen et al. 2017). Most

recently, Nguyen et al. (2017) used the velocity field derived from the CO bandhead feature observed with the Gemini/NIFS IFS to derive an upper limit on the mass of the putative central BH. While deriving a BH mass from the data presented here is outside the scope of this work, we do find a stellar velocity field consistent with these prior studies when considering the smaller field of view of the OSIRIS data.

The CO bandhead stellar absorption feature present in the Kbb data cube can be used to constrain the dominant age of the central stellar population in NGC 404. This absorption feature is sensitive to intermediate-age stellar populations because the CO bandheads are stronger in cooler stars with lower surface gravity (i.e., giant and supergiant stars) than in dwarf stars. The strength of the absorption feature is often characterized by the CO index. We employed the CO index defined by Mármol-Queraltó et al. (2008), $D_{\rm CO}$. That work found the $D_{\rm CO}$ index to be less sensitive to velocity dispersion, RV, and low-S/N spectra than previously defined CO indices. Here $D_{\rm CO}$ is computed by taking a ratio of the average flux in two continuum bands (2.2460–2.2550 and 2.2710–2.2770 μm) over the average flux in one absorption band (2.2880–2.3010 μm), such that a $D_{\rm CO}$ value of $\sim$1 indicates no CO absorption and increasing values indicate a deeper CO absorption depth relative to the continuum. For reference, individual dwarf stars have $D_{\rm CO}$ values ranging from $\sim$1 to 1.1, red supergiants have values of $\sim$1.2–1.25, and AGB stars have values up to $\sim$1.3.

The $D_{\rm CO}$ index in the nucleus of NGC 404 was computed for each individual spaxel of the Kbb data cube by first shifting the wavelength ranges of the continuum and absorption bands to the systemic velocity of NGC 404. The radial dependence of the CO index was also probed by taking the average of the CO index in 0″1 (1.5 pc) wide radial bins from 0 to 0″5 (7.5 pc). The error in each radial bin was taken as the error of the mean (standard deviation divided by a square root of the number of pixels contributing to the average). The resulting map and radial dependence of the $D_{\rm CO}$ index is shown in Figure 11 for spaxels with a continuum S/N greater than 7.0. We measure a significant spatial variation of the CO index with a value of 1.168 ± 0.003 at the center of NGC 404 and increasing to values of $\sim$1.195 ($\sim$25% more CO absorption) at 5–7 pc from the Kbb continuum center.

The strength of the CO absorption quantified by the $D_{\rm CO}$ index can be interpreted by comparing indices measured on the spectra of a simulated stellar population with the indices measured from the data, thereby constraining the age of the stellar population. Meneses-Goytia et al. (2015) performed single age and metallicity stellar population synthesis modeling in the NIR based on empirical stellar spectra from the IRTF spectral library (Rayner et al. 2009). That work computed a number of spectral indices and tracked their values as a function of age (from 1 to 14 Gyr) and metallicity (-0.70 to $+0.20$ dex relative to solar) of the stellar population. Note that

Aperture Number	Line Fluxes (counts)				Line Flux Error (counts)	1–0 S(2)/ 1–0 S(0)	2–1 S(1)/ 1–0 S(1)
	1–0 S(2)	1–0 S(1)	1–0 S(0)	2–1 S(1)			
1	0.09	0.33	0.15	<0.10	0.03	1.7 ± 0.6	<0.30
2	0.029	0.089	0.042	<0.020	0.007	1.5 ± 0.4	<0.23
3	0.016	0.049	0.030	0.012	0.004	1.9 ± 0.5	0.25 ± 0.09
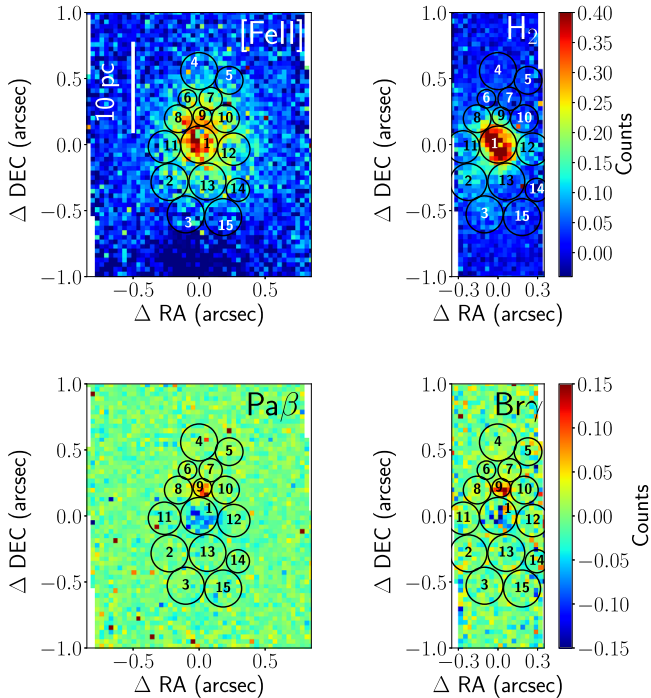
Figure 9. Circular apertures in which the [Fe II]/Paβ and 1–0 S(1) H$_2$/Brγ are estimated, overplotted on the [Fe II], Paβ, 1–0 S(1) H$_2$, and Brγ emission-line maps from Figure 3. Apertures 1, 2, and 3 are the same apertures used in the H$_2$ line ratio measurements described in Section 3.6. Aperture 9 was chosen to be centered on the peak of Paβ/Brγ to the north of the NGC 404 nucleus. Other apertures were used to fill in the remaining area of the [Fe II] emission, the most spatially extended emission line. The radii of the apertures vary from 2–4 pixels (1–2 pc).

earlier ages were not modeled due to the lack of high-temperature main-sequence stars in the IRTF spectral library.

When comparing the measured D_{CO} values to the simulated values (Figure 11 in Meneses-Goytia et al. 2015), we find that the D_{CO} value at the nucleus of 1.168 ± 0.003 is lower than most of the computed models and can only be produced by a stellar population with an age of 1–1.5 Gyr and a metallicity of 0 to +0.2 dex relative to solar. The higher value of ~1.195 found at larger radii from the nucleus is reproduced by a larger set of models with ages ranging from 1 to 7 Gyr and metallicities spanning the full sampled range. The dominant stellar population age of 1–1.5 Gyr that we find in the central 1.5 pc of NGC 404 is consistent with previous results using optical spectroscopy (e.g., Seth et al. 2010; Nguyen et al. 2017).

We also consider the constraints that the Paβ absorption feature observed in the central ~4 pc of NGC 404 places on the stellar population. This absorption feature can be affected by contamination of emission, unlike the CO bandheads, but it is still interesting to explore the possible stellar population ages consistent with the measurement of this feature's equivalent

width (EW). Since stellar population models such as that of Meneses-Goytia et al. (2015) do not give predictions for Paβ EW versus age, we compared the measured EW in a spatial aperture centered on the nucleus of NGC 404 with a 2 pc radius (aperture 1 in Figures 8 and 9) to those measured from the telluric standard spectra of A0V and G2V stars (see Section 2) and other dwarf stars ranging from spectral type F to M stars from the IRTF spectral library (Rayner et al. 2009). We find an EW consistent with a stellar population dominated in the NIR by late-F/early-G stars or late-B stars. Based on the main-sequence lifetimes of these stars, this Paβ EW implies the presence of stars with an age of <5–8 Gyr, consistent with our CO bandhead constraints, or a young stellar population with an age of <500 Myr. We also compared the measured EW to that of a nominal old stellar population dominated by K0 stars to determine what fraction of A stars is needed to reproduce the measured Paβ absorption. Using the Paβ EW of K0 and A0 stars and adopting the relative J-band magnitudes of these stars from Pecaut & Mamajek (2013),[8] we find that an A star number fraction of ~1% (equivalent to a mass fraction of ~4%) is required to reproduce the measured EW. This result suggests that there is a young component in the nuclear stellar population of NGC 404 in addition to the ~1 Gyr component indicated by the CO bandhead absorption. The previous optical spectroscopic studies mentioned above have also found a component of young stars in the nucleus of NGC 404, with the preferred stellar population model in the most recent work finding that this young component (<500 Myr) is a small fraction of the total mass (~6%) compared to the 1 Gyr stars (Nguyen et al. 2017). Those authors also pointed out a region of blue optical colors slightly offset to the west of the nucleus that they attributed to this young stellar population, which coincides with the Paβ absorption seen in the velocity-resolved emission maps offset ~1 pc to the west of the nucleus (see the 50 and 100 km s^{-1} velocity channels in Figure 4). Another sign of the presence of younger stars in this region is the Paβ/Brγ emission seen 3 pc to the north of the nucleus of NGC 404. This compact clump of hydrogen recombination emission is spatially coincident with bright, extended [Fe II] emission (see the 50 km s^{-1} channel in Figure 4) and likely originates from an H II region powered by star formation.

4.2. Molecular Hydrogen Gas Disk

The nuclear molecular gas in NGC 404 is observed through the H$_2$ ro-vibration emission lines. In this emission line, we observe a central peak of emission in the central ~5 pc that is coincident with the peak of the stellar infrared continuum, as well as clumps of emission to the southeast of the continuum peak that are either physically separate knots of molecular gas or hot spots in a larger rotating disk. The H$_2$ velocity profile is

---

[8] See also http://www.pas.rochester.edu/~emamajek/EEM_dwarf_UBVIJHK_colors_Teff.txt.

Table 3
[Fe II]/Paβ and 1–0 S(1)/Brγ Line Ratio Measurements in NGC 404

Aperture Number	Aperture Location (arcsec)		Radius (pixels)	Velocity Ranges (km s^{-1})[a]		Line Fluxes (×10^2 counts)				[Fe II]/ Paβ[c]	1–0 S(1) H$_2$/Brγ[c]
	(ΔR.A.)	(Δdecl.)		Line Flux	Continuum[b]	[Fe II]	Paβ	1–0 S(1) H$_2$	Brγ		
1	0.00	0.00	4.0	±250	300–450	15	⋯	38	⋯	⋯	⋯
2	−0.22	−0.28	4.0	±200	200–350	5.0	⋯	9.9	⋯	⋯	⋯
3	−0.10	−0.53	4.0	±175	175–325	2.3	0.5	5.5	<2.2	4.3	>2.6
4	0.00	0.56	4.0	±250	300–450	4.4	0.8	3.6	1.3	5.7	2.7
5	0.23	0.49	3.0	±250	300–450	4.1	0.6	4.6	<3.4	6.4	>1.4
6	−0.09	0.35	2.0	±250	300–450	8.4	1.4	4.2	<3.8	6.0	>1.1
7	0.09	0.35	2.5	±250	300–450	9.6	1.8	4.3	1.7	5.3	2.4
8	−0.16	0.20	3.0	±250	300–450	10	1.6	13	<4.5	6.5	>2.8
9	0.02	0.21	2.0	±250	300–450	13	5.4	12	11	2.5	1.2
10	0.20	0.20	3.0	±175	175–325	7.2	1.4	4.0	<5.1	5.3	>0.8
11	−0.26	−0.02	3.5	±250	300–450	5.9	⋯	8.4	⋯	⋯	⋯
12	0.26	−0.04	3.5	±250	300–450	7.7	⋯	9.2	⋯	⋯	⋯
13	0.06	−0.28	4.0	±250	300–450	8.2	⋯	9.6	⋯	⋯	⋯
14	0.29	−0.34	2.5	±200	200–350	5.1	⋯	3.2	⋯	⋯	⋯
15	0.18	−0.55	4.0	±175	175–325	2.1	0.5	2.6	<3.0	3.8	>0.9

Notes.
[a] All velocity values are relative to the systemic velocity of the galaxy (−48 km sec^{-1}).
[b] The continuum velocity range given here refers to both the red (e.g., +300 to +450 km s^{-1}) and blue (e.g., −450 to −300 km s^{-1}) sides of the emission line. Wavelength channels in these two ranges are used to estimate the continuum.
[c] Line ratio measurements/upper limits are not reported for spectra with measured Paβ absorption.

distinct from the stellar velocities (Figure 7) and shows signs of rotation at a position angle of −45° spanning line-of-sight velocities of ±30 km s^{-1} across both the central and offset clumps of H$_2$ line emission (Figure 5). Similar to the stellar velocities derived from the CO bandhead, the molecular gas velocities have previously been used to constrain the mass of the possible central BH (Seth et al. 2010), although a more recent work found that the kinematics are dominated by nongravitational motions and thus do not give a reliable BH mass measurement (Nguyen et al. 2017). We find H$_2$ gas velocities in the OSIRIS data that are consistent with the H$_2$ velocity maps derived from the Gemini/NIFS data presented in those previous works.

The dominant excitation mechanism of the H$_2$ molecular gas can be constrained by comparing H$_2$ line ratios derived in Section 3.6 to models. These line ratios can also be converted to two excitation temperatures: the rotation temperature ($T_{\rm rot}$, derived from the 1–0 S(2)/1–0 S(0) ratio) and the vibrational temperature ($T_{\rm vib}$, derived from the 1–0 S(1)/2–1 S(1) ratio). We applied the equations from Reunanen et al. (2002), which assume local thermal equilibrium and therefore a thermal distribution for the ro-vibrational level populations:

$$T_{\rm rot} = \frac{-1113}{\ln\left(0.323 \times \frac{1\text{-}0S(2)}{1\text{-}0S(0)}\right)}, \quad (1)$$

$$T_{\rm vib} = \frac{5600}{\ln\left(1.355 \times \frac{1\text{-}0S(1)}{2\text{-}1S(1)}\right)}. \quad (2)$$

In the case of purely thermal (collisional) excitation, the molecular gas is in local thermal equilibrium, and the level populations are set by a Boltzmann distribution. The two excitation temperatures are therefore equal to each other and to the kinetic temperature of the gas. For UV fluorescence excitation, the upper energy levels of the H$_2$ are overpopulated

compared to the Boltzmann distribution due to the absorption of UV photons, resulting in a higher $T_{\rm vib}$ ratio compared to $T_{\rm rot}$ by a factor of ~6 (Black & van Dishoeck 1987).

We compare the measured line ratios of 2–1 S(1)/1–0 S(1) and 1–0 S(2)/1–0 S(0) and the corresponding excitation temperatures of $T_{\rm vib}$ and $T_{\rm rot}$ in each of the three spatial apertures in NGC 404 in Figure 12 (Mouri 1994). These measurements were compared to expected values for thermal excitation ($T_{\rm vib} = T_{\rm rot}$) and UV fluorescence excitation ($T_{\rm vib}$ much greater than $T_{\rm rot}$; Black & van Dishoeck 1987). We measured consistent line ratios and excitation temperatures within the three spatial apertures centered on the central bright H$_2$ emission and the two peaks of emission offset to the southeast of the nucleus. In the 2–1 S(1)/1–0 S(1) versus 1–0 S(2)/1–0 S(0) parameter space in Figure 12, the line ratio measurements and/or upper limits in each aperture fall near the thermal excitation curve of $T_{\rm vib} = T_{\rm rot}$ with an offset toward the UV fluorescence excitation models. We therefore conclude that the H$_2$ excitation mechanism is consistent with thermal excitation at all three spatial locations, with a temperature of 2000–4000 K plus some contribution of UV fluorescent excitation. Given the kinematic and morphological structure of the H$_2$ emission, we interpret the central peak of emission as a rotating disk of thermally excited molecular gas. Thermally excited disks of H$_2$ gas have been commonly found at the centers of classical Seyferts (e.g., Hicks et al. 2009, 2013; Storchi-Bergmann et al. 2009; Riffel et al. 2015; Hicks et al. 2016), as well as optically classified LINERs and low-luminosity AGNs (e.g., Mazzalay et al. 2013, 2014; Müller-Sánchez et al. 2013). The peaks of offset H$_2$ emission are also dominated by thermal excitation, but it is unclear whether these peaks trace hot spots in a larger-scale rotating disk associated with the central emission peak or are physically separate clumps of gas.

Although we can determine that the H$_2$ gas in NGC 404 is dominated by thermal excitation, it is more difficult to constrain
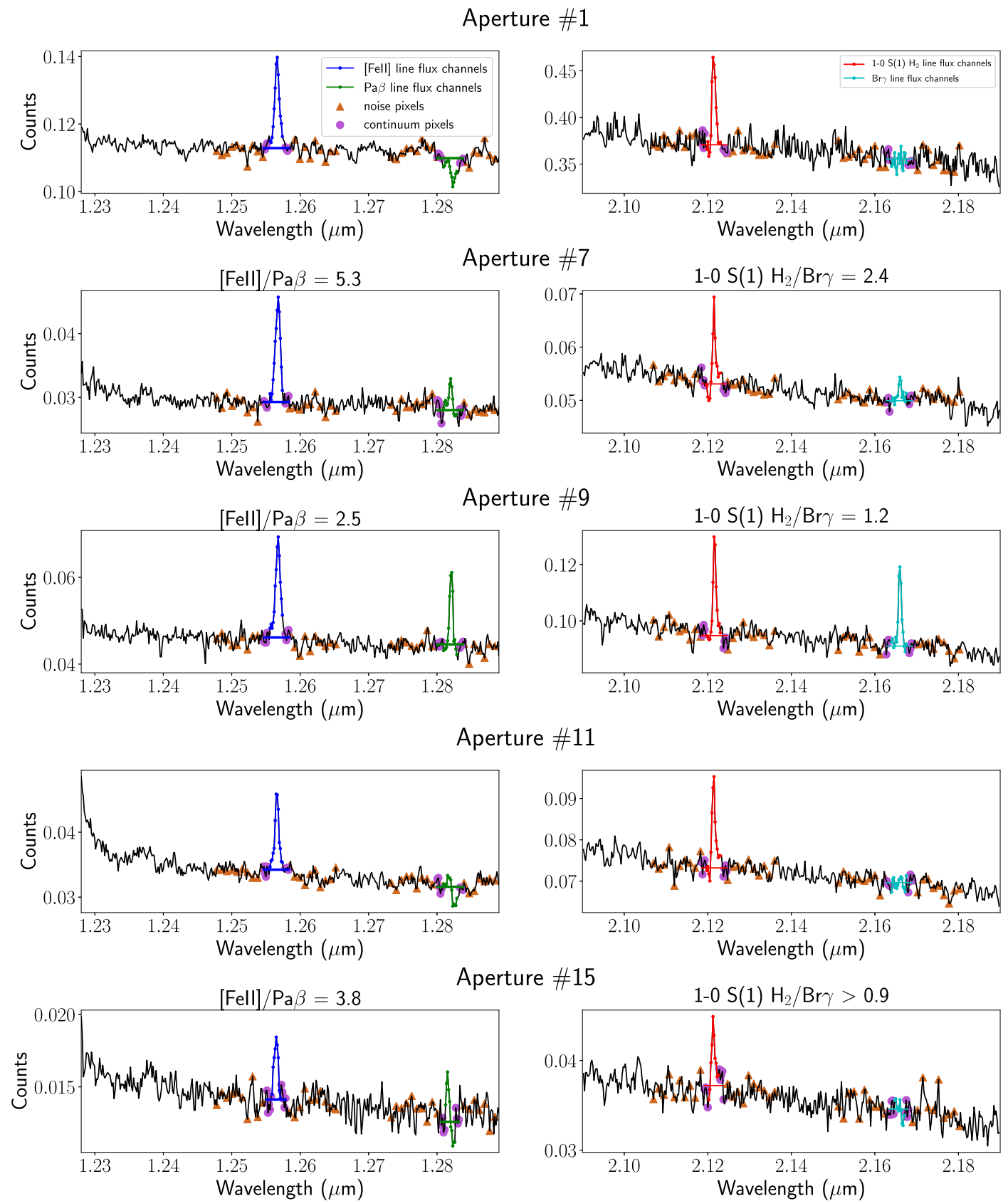
Figure 10. Example spectra to represent the variety of emission-line morphologies and ratios observed in NGC 404. The overall spectrum is plotted in black, and each emission line is plotted in a different color to indicate the wavelength channels used to measure the line flux. The pixels used for both the noise and the continuum estimation are shown as brown triangles and purple circles, respectively. The continuum estimation is also plotted as a horizontal line spanning the channels used for both the continuum and line-flux measurements. The spectra plotted here show examples of high (7) and low (9) [Fe II]/Paβ and H$_2$/Brγ line ratios, a region in which Paβ is detected but only a limit can be placed on Brγ (15), and regions of strong (1) and weak (11) Paβ absorption in which the line ratios are not constrained.
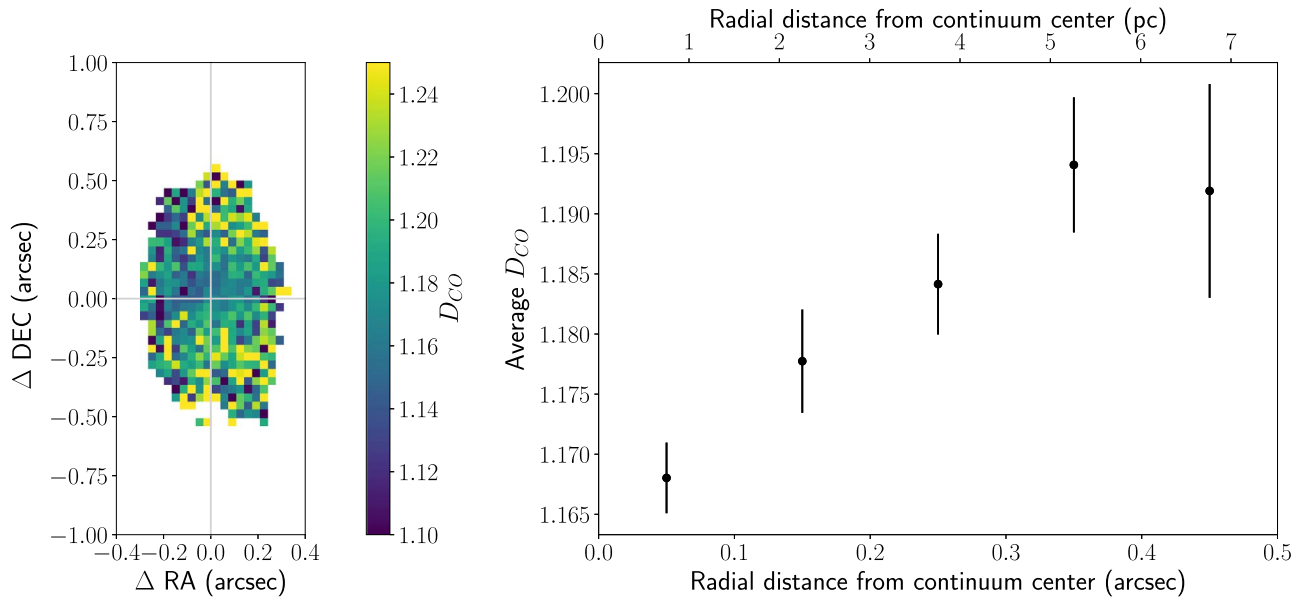
Figure 11. Map of the CO index $D_{\rm CO}$ across the central $\sim$0.5 × 1″.0 (7.5 × 15 pc) of the nucleus of NGC 404 (left) and $D_{\rm CO}$ vs. radius (right). In the spatial map, only the spaxels with a continuum S/N greater than 7.0 are displayed. The origin of the map is set to the center of the Kbb continuum emission and highlighted by the horizontal and vertical gray lines. The $D_{\rm CO}$ index in the nucleus of NGC 404 has a value of 1.168 ± 0.003 at the center and increases to a value of $\sim$1.195, or $\sim$25% more CO absorption, at distances of ±5–7 pc from the center.
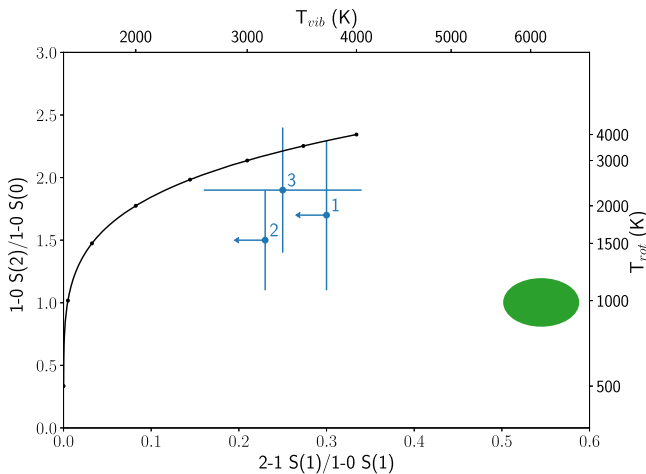
Figure 12. The 2–1 S(1)/1–0 S(1) vs. 1–0 S(2)/1–0 S(0) H_2 line ratios for each of the three spatial apertures displayed in Figure 8 (Mouri 1994). The excitation temperatures $T_{\rm rot}$ and $T_{\rm vib}$ calculated from each line ratio are also shown on the top and right axes. The black curve shows the line ratios and temperatures corresponding to thermal excitation ($T_{\rm rot} = T_{\rm vib}$) for gas temperatures ranging from 500 to 4000 K, with black points having a spacing of 500 K. The green ellipse covers the range of H_2 spectral models from UV fluorescence excitation from Black & van Dishoeck (1987). The line ratios in the three apertures are all consistent with each other and fall near the thermal excitation curve at temperatures of 2000–4000 K with a slight shift toward the UV fluorescence models. These results indicate that the H_2 gas in NGC 404 is thermally excited, with some contribution from UV fluorescence.

the physical mechanism heating the H_2 gas from the line ratios alone. One possibility is that the H_2 is being heated by the same shock front that is exciting the [Fe II] emission as these shocks impinge on the central disk of molecular gas (discussed in detail in Section 4.3). Other potential heating sources include UV radiation from young stars or X-ray radiation from X-ray binaries or the central weakly accreting BH. To explore what might be heating the gas, we constrained the mass of the warm H_2 gas and its total internal energy. We used the equation presented in Mazzalay et al. (2013) to convert the 1–0 S(1) line

flux to the warm H_2 gas mass (M_{H_2}), which assumes a kinetic gas temperature of 2000 K:

$$M_{H_2} \simeq 5.0875 \times 10^{13} \left(\frac{D}{\rm Mpc}\right)^2$$
$$\times \left(\frac{1 - 0 S(1)}{\rm erg\ s^{-1}\ cm^{-2}}\right) 10^{0.4 \times A_{2.2}}. \tag{3}$$

In this equation, D is the distance to the galaxy (3.1 Mpc for NGC 404) and $A_{2.2}$ is the extinction at 2.2 μm. We used the 1–0 S(1) H_2 line flux presented in Larkin et al. (1998) for the central $\sim$10 × 45 pc of NGC 404 and assumed a large value of 1.0 for $A_{2.2}$ (corresponding to a visible extinction A_V of $\sim$10.0) to find a conservative upper limit for the H_2 gas mass. The resulting maximum warm molecular gas mass in the nucleus of NGC 404 is 3 $M_\odot$. This warm H_2 mass is comparable to masses derived by Mazzalay et al. (2013) for a sample of six nearby galaxies that exhibit a range of nuclear activity when taking into account the different spatial scales probed by those data compared to Larkin et al. (1998). Note that this is only a measurement of the mass of the gas that is warm and emitting the thermally exciting lines; it does not include the cold H_2 gas, which is expected to be a factor of 10^5–10^7 higher than the warm gas mass (see Dale et al. 2005; Müller-Sánchez et al. 2006). The warm H_2 mass can then be converted to the total internal energy using $U = c_P n T$, where c_P is the specific heat at a constant pressure of H_2, n is the number of moles of H_2, and T is the gas kinetic temperature of 2000 K. Given a value of c_P at 2000 K of 34 J/(K mol) from the NIST Standard Reference Database, we find an upper limit for the total internal energy of the H_2 gas of 2 × 10^{45} erg. This total energy is six orders of magnitude lower than the total kinetic energy released by a single supernova. This low value of the total warm H_2 energy suggests that there are many possible physical
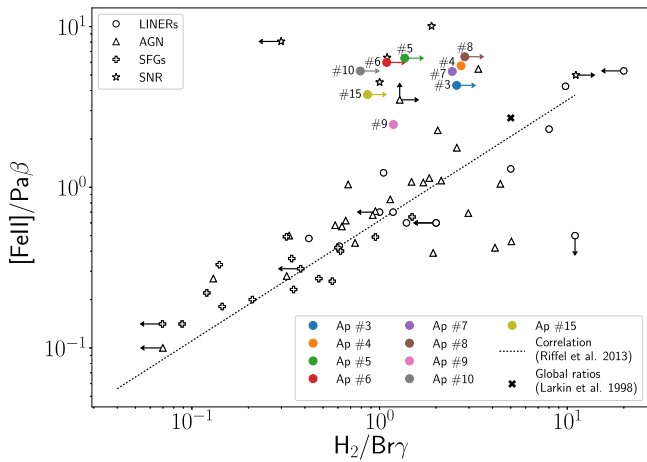
Figure 13. Plot of the [Fe II]/Paβ and 1–0 S(1) H₂/Brγ emission-line ratio measurements and lower limits for different spatial apertures. Apertures in which Paβ absorption is detected are not plotted. The correlation between these two line ratios as measured from spatially integrated slit spectra of AGNs, star-forming galaxies (SFGs), and LINER galaxies is shown as a black dashed line (Riffel et al. 2013). Values from individual sources in the literature are plotted for LINERs, SFGs, AGNs, and supernova remnants (SNRs; Larkin et al. 1998; Dale et al. 2004; Rodríguez-Ardila et al. 2004, 2005; Riffel et al. 2013). The global line ratios for NGC 404 from Larkin et al. (1998) are plotted as a black cross. We find that the line ratios in NGC 404 measured by OSIRIS are generally 1.5–2.5 times higher than the global line ratios measured by Larkin et al. (1998) and fall near the shocked regions of SNRs in this parameter space. The aperture centered on the Paβ/Brγ emission (aperture 9) is lower than the other apertures and consistent with the global line ratios. The high line ratios measured by OSIRIS are evidence that the [Fe II] emission in NGC 404 is excited by widespread shocks in the nucleus of this galaxy.

mechanisms, including the supernova remnant shock, that could contribute to the heating of the gas and thereby cause the thermal excitation that we observe.

4.3. Shock Front Traced by [Fe II] Gas Emission

The [Fe II] line emission has a distinct morphology and velocity profile from the stellar continuum and the molecular gas in the nucleus of NGC 404. The emission from this ionized gas is spatially extended across the central ∼15 pc of the nucleus and follows a complex velocity structure that spans a wide range of velocities down to $-150\,\mathrm{km\,s^{-1}}$ and up to $+200\,\mathrm{km\,s^{-1}}$ (Figure 4). A key constraint on the important physical mechanisms in the nucleus of NGC 404 is through this shock-sensitive emission line, particularly the ratio of the [Fe II] line flux over Paβ. We argue below that the [Fe II] emission is excited by shocks and might be tracing a shock front caused by a supernova.

Constraints on the physical mechanism that excites the [Fe II] emission in NGC 404 can be made using measurements of the [Fe II]/Paβ ratio (Section 3.7). High values of this ratio (>2.0) are indicative of shock excitation, which can efficiently destroy/ablate dust grains and thereby increase the gas-phase abundance of iron, which is typically highly depleted in the interstellar medium (Blietz et al. 1994; Larkin et al. 1998). Figure 13 plots the [Fe II]/Paβ and H₂/Brγ line ratios presented in Table 3. These measurements, which probe physical scales of 1–2 pc, are compared to values in other objects from the literature and the overall correlation found in these line ratios from spatially integrated spectra of starburst, AGN, and LINER galaxies (Larkin et al. 1998; Riffel et al. 2013). The global line ratios for NGC 404 derived by

Larkin et al. (1998) from slit spectra that cover the central ∼10 × 45 pc are also plotted. We find that the [Fe II]/Paβ line ratio measured in the small apertures with OSIRIS is generally 1.5–2.5 times higher than the global [Fe II]/Paβ ratio measured by Larkin et al. (1998). The aperture centered on the Paβ/Brγ emission feature (9) has an [Fe II]/Paβ line ratio that is lower than the rest of the spatial locations and consistent with the global ratio. The high [Fe II]/Paβ values ranging from 4 to 6.5 are among the highest measured in extragalactic sources and are similar to those seen in the shocked regions of supernova remnants, also plotted in Figure 13. From these high [Fe II]/Paβ ratios, we conclude that the [Fe II] emission in NGC 404 is due to shock excitation.

One possible source of the shocks that excite the [Fe II] emission is one or more supernova remnants. Larkin et al. (1998) previously suggested this scenario for NGC 404's [Fe II] emission and found that the [Fe II] emission seen in the central ∼10 × 45 pc is only a few times that produced by a single supernova remnant. Pogge et al. (2000) also noted that the extended, bubble-like structure of [N II]+Hα emission seen in *HST* optical narrowband imaging is similar to that of a supernova remnant. In comparing the [N II]+Hα imaging data to the [Fe II] emission at $-50\,\mathrm{km\,s^{-1}}$, we find that the curvatures and spatial extension of the [Fe II] emission to the north and southwest of the nucleus are very similar to the [N II]+Hα structure (see Figure 14). The similarity between these morphologies and the high [Fe II]/Paβ ratios suggests that the [Fe II] emission originates from a shock front caused by one or more supernovae that were offset to the west of the nucleus by ∼5 pc (i.e., the location of the center of the [N II]+Hα bubble seen in the *HST* data). As this shock front reaches the denser gas in the nucleus, it can excite the [Fe II] emission and produce the observed [Fe II]/Paβ ratios.

A supernova remnant was previously considered by Nyland et al. (2012) as a possible source of the observed radio and hard X-ray (2–10 keV; Binder et al. 2011) nuclear emission in NGC 404. That work explored a core-collapse supernova as the original source of the remnant and argued that this scenario was statistically unlikely given the current star formation rate. It is also possible, however, that the supernova causing the observed [Fe II]-exciting shocks was instead a Type Ia (SN Ia), which would be more consistent with the dominant stellar population age of ∼1 Gyr found in this work (see Section 4.1) and in previous optical studies of the nucleus of NGC 404 at seeing-limited (Fernandes et al. 2004; Bouchard et al. 2010) and diffraction-limited (Seth et al. 2010; Nguyen et al. 2017) angular resolutions. For the nuclear star cluster mass from Nguyen et al. (2017) of $1.2 \times 10^7\,M_\odot$ and the dominant age of ∼1 Gyr, the expected current rate of SNe Ia is ∼5 every 1 Myr (Maoz & Mannucci 2012). Given this current rate of SNe Ia and assuming a lifetime of a supernova remnant on order 10,000–100,000 yr, we used the Poisson distribution to calculate the probability that a supernova occurred in the last 10,000–100,000 yr to be 5%–30%. It is therefore possible that we are currently observing a SN Ia remnant in the nucleus of NGC 404, and we argue that the dominant source of the shocks exciting the [Fe II] emission could be due to such a supernova.

5. Summary

We have presented the first spatially resolved data of *J*-band [Fe II] and Paβ emission in the nucleus of NGC 404 and compared it to the *K*-band H₂ and Brγ emission and CO stellar
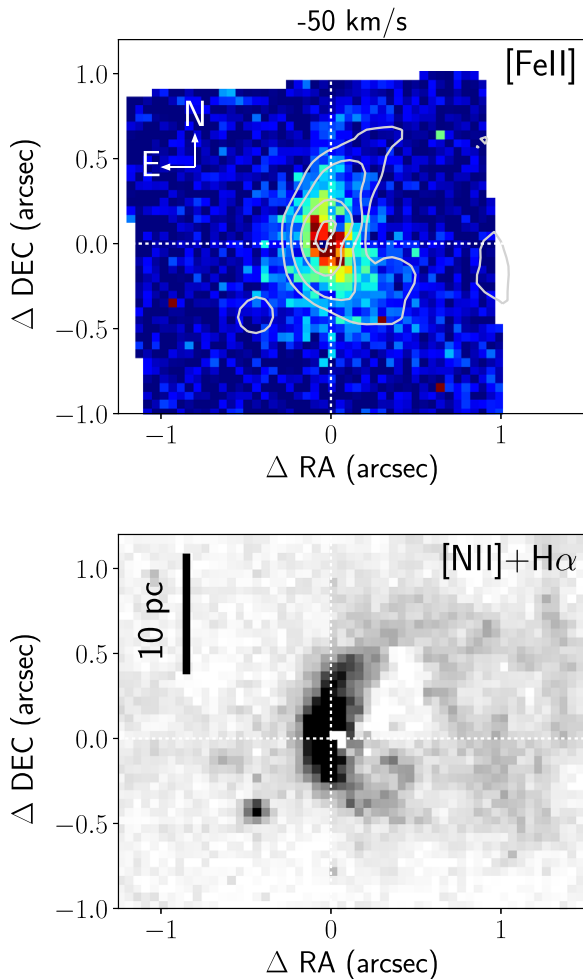
Figure 14. Comparison of the [Fe II] emission morphology observed at −50 km s⁻¹ relative to the systemic velocity of the galaxy (this work; see Section 3.3) and the [N II]+Hα emission observed using *HST* narrowband imaging (Pogge et al. 2000). The origin of each plot is set to the continuum center as determined by a Gaussian fit to the spectrally averaged Jn2 data cube (top) and the F547M continuum filter image (bottom). The [Fe II] emission map was derived from the OSIRIS data taken in the 50 mas plate scale mode (see Section 2 for details). Contours of the [N II] + Hα image are overplotted on the [Fe II] map, highlighting that the curvature and spatial extension of the [Fe II] emission at this velocity are similar to the [N II] + Hα structure. Based on these similarities and the very high [Fe II]/Paβ ratios observed in NGC 404, we argue that the [Fe II] emission may be excited by shocks originating from a supernova that occurred at the center of the [N II] + Hα bubble ∼5 pc to the west and is now impinging on the central dense gas in the nucleus of NGC 404.

absorption. These high angular resolution data reveal differences in the morphology and kinematics of the stars and the ionized and molecular gas at pc spatial scales in this LINER nucleus. We find that the data are best explained by at least four physical components: a nuclear star cluster, an H II region, a thermally excited rotating molecular gas disk, and a shock front traced by the [Fe II] emission. We summarize our results related to these physical components below.

1. *Stellar population and* H II *region*. We observed infrared continuum and CO, Paβ, and Brγ absorption features from the nuclear stellar population. We used the depth of the CO absorption feature, quantified by the CO index, to constrain the stellar population and find a dominant age of ∼1 Gyr at the center of NGC 404, with a wider range of possible ages from 1 to 7 Gyr at increasing radii. We

also identified a region of Paβ and Brγ emission 3 pc north of the nucleus that is likely an H II region powered by star formation.

2. H₂ *gas disk*. The H₂ gas emission primarily originates from a central rotating disk whose emission spans the central ∼5 pc of the nucleus. This disk is rotating at a position angle of −45° on the sky with line-of-sight rotation speeds up to ±30 km s⁻¹. We also find extended H₂ emission to the southeast of the nucleus that may originate from physically separate knots of gas or hot spots in the rotating disk. Ratios of the observed ro-vibration emission lines indicate that all of the observed molecular gas emission is thermally excited with some contribution from UV fluorescence. The exact source of the heating is not well constrained, but we find that a single supernova has six orders of magnitude more energy than required to have heated the gas to its current temperature.

3. [Fe II]*-traced shock front*. The observed [Fe II] emission extends across the central ∼15 pc of the nucleus and has a complex velocity structure spanning out to −150 and 200 km s⁻¹. High [Fe II]/Paβ line ratios across the spatial extent of this emission provide strong evidence that the [Fe II] emission is excited by shocks. We argue that a possible physical source of the [Fe II] shock excitation is a supernova remnant. This scenario is supported by both the high [Fe II]/Paβ ratios similar to the shocked regions of supernova remnants (Figure 13) and the similar morphology of [Fe II] and [N II]+Hα from *HST* narrowband imaging (Figure 14; Pogge et al. 2000). So, although we cannot rule out a contribution from the accreting intermediate-mass BH at the center of NGC 404, we conclude that a single SN could be responsible for the shock-excited LINER emission at NIR wavelengths.

ORCID iDs

A. Boehle ⓘ https://orcid.org/0000-0003-0439-7634
J. E. Larkin ⓘ https://orcid.org/0000-0001-7687-3965
L. Armus ⓘ https://orcid.org/0000-0003-3498-2973

References

Binder, B., Williams, B. F., Eracleous, M., et al. 2011, ApJ, 737, 77
Black, J. H., & van Dishoeck, E. F. 1987, ApJ, 322, 412
Blietz, M., Cameron, M., Drapatz, S., et al. 1994, ApJ, 421, 92
Bouchard, A., Prugniel, P., Koleva, M., & Sharina, M. 2010, A&A, 513, A54
Dale, D. A., Bendo, G. J., Engelbracht, C. W., et al. 2005, ApJ, 633, 857
Dale, D. A., Roussel, H., Contursi, A., et al. 2004, ApJ, 601, 813

Davies, R. I. 2007, MNRAS, 375, 1099

Fernandes, R. C., Delgado, R. M. G., Schmitt, H., et al. 2004, ApJ, 605, 105

González Delgado, R. M., Pérez, E., Cid Fernandes, R., & Schmitt, H. 2008, AJ, 135, 747

Heckman, T. M. 1980, A&A, 87, 152

Hicks, E. K. S., Davies, R. I., Maciejewski, W., et al. 2013, ApJ, 768, 107

Hicks, E. K. S., Davies, R. I., Malkan, M. A., et al. 2009, ApJ, 696, 448

Hicks, E. K. S., Müller-Sánchez, F., Malkan, M. A., & Yu, P.-C. 2016, in IAU Symp. 319, Galaxies at High Redshift and Their Evolution Over Cosmic Time, ed. S. Kaviraj (Paris: IAU), 59

Ho, L. C., Filippenko, A. V., & Sargent, W. L. W. 1997a, ApJS, 112, 315

Ho, L. C., Filippenko, A. V., & Sargent, W. L. W. 1997b, ApJ, 487, 568

Krabbe, A., Gasaway, T., Song, I., et al. 2004, Proc. SPIE, 5492, 1403

Larkin, J., Barczys, M., Krabbe, A., et al. 2006, NewAR, 50, 362

Larkin, J. E., Armus, L., Knop, R. A., Soifer, B. T., & Matthews, K. 1998, ApJS, 114, 59

Lee, M. G., & Jang, I. S. 2016, ApJ, 822, 70

Maoz, D., & Mannucci, F. 2012, PASA, 29, 447

Maoz, D., Nagar, N. M., Falcke, H., & Wilson, A. S. 2005, ApJ, 625, 699

Mármol-Queraltó, E., Cardiel, N., Cenarro, A. J., et al. 2008, A&A, 489, 885

Mazzalay, X., Maciejewski, W., Erwin, P., et al. 2014, MNRAS, 438, 2036

Mazzalay, X., Saglia, R. P., Erwin, P., et al. 2013, MNRAS, 428, 2389

Meneses-Goytia, S., Peletier, R. F., Trager, S. C., & Vazdekis, A. 2015, A&A, 582, A97

Mouri, H. 1994, ApJ, 427, 777

Müller Sánchez, F., Davies, R. I., Eisenhauer, F., et al. 2006, A&A, 454, 481

Müller-Sánchez, F., Prieto, M. A., Mezcua, M., et al. 2013, ApJL, 763, L1

Nguyen, D. D., Seth, A. C., den Brok, M., et al. 2017, ApJ, 836, 237

Nyland, K., Davis, T. A., Nguyen, D. D., et al. 2017, ApJ, 845, 50

Nyland, K., Marvil, J., Wrobel, J. M., Young, L. M., & Zauderer, B. A. 2012, ApJ, 753, 103

Pecaut, M. J., & Mamajek, E. E. 2013, ApJS, 208, 9

Pogge, R. W., Maoz, D., Ho, L. C., & Eracleous, M. 2000, ApJ, 532, 323

Ravindranath, S., Ho, L. C., Peng, C. Y., Filippenko, A. V., & Sargent, W. L. W. 2001, AJ, 122, 653

Rayner, J. T., Cushing, M. C., & Vacca, W. D. 2009, ApJS, 185, 289

Reunanen, J., Kotilainen, J. K., & Prieto, M. A. 2002, MNRAS, 331, 154

Riffel, R., Rodríguez-Ardila, A., Aleman, I., et al. 2013, MNRAS, 430, 2002

Riffel, R. A., Storchi-Bergmann, T., & Riffel, R. 2015, MNRAS, 451, 3587

Rodríguez-Ardila, A., Pastoriza, M. G., Viegas, S., Sigut, T. A. A., & Pradhan, A. K. 2004, A&A, 425, 457

Rodríguez-Ardila, A., Riffel, R., & Pastoriza, M. G. 2005, MNRAS, 364, 1041

Seth, A. C., Cappellari, M., Neumayer, N., et al. 2010, ApJ, 714, 713

Stoehr, F., White, R., Smith, M., et al. 2008, in ASP Conf. Ser. 394, Astronomical Data Analysis Software and Systems XVII, ed. R. W. Argyle, P. S. Bunclark, & J. R. Lewis (San Francisco, CA: ASP), 505

Storchi-Bergmann, T., McGregor, P. J., Riffel, R. A., et al. 2009, MNRAS, 394, 1148

van Dam, M. A., Bouchez, A. H., Le Mignant, D., et al. 2006, PASP, 118, 310

Wizinowich, P. L., Le Mignant, D., Bouchez, A. H., et al. 2006, PASP, 118, 297